Sensors & Actuators: B. Chemical 427 (2025) 137195

Contents lists available at ScienceDirect

Sensors and Actuators: B. Chemical

journal homepage: www.elsevier.com/locate/snb

An ultrasensitive lateral flow strip assay based on MXene@PtCu nanozymes for visual biosensing of *Burkholderia pseudomallei* EV-sRNA

Jun Tan [a,1], Nini Luo [a,1], Ting Zhang [a,1], Juan Yao [a], Xuemiao Li [a], Yanshuang Wang [d], Guozhen Tian [e], Hua Pei [d], Qizhi Diao [c,*], Huangxian Ju [b,*], Qianfeng Xia [a,*]

[a] NHC Key Laboratory of Tropical Disease Control, School of Tropical Medicine, Hainan Medical University, Haikou, Hainan 571199, China
[b] State Key Laboratory of Analytical Chemistry for Life Science, School of Chemistry and Chemical Engineering, Nanjing University, Nanjing 210023, China
[c] Hainan Branch, Shanghai Children's Medical Center, School of Medicine, Shanghai Jiao Tong University, Sanya 572000, China
[d] The Second Affiliated Hospital, Hainan Medical University, Haikou, Hainan 571199, China
[e] Hainan Women and Children's Medical Center, Haikou, Hainan 571199, China

ARTICLE INFO

Keywords:
Burkholderia pseudomallei
Extracellular vesicles
Biosensors
MXene@PtCu nanoenzyme
Visual detection

ABSTRACT

Burkholderia pseudomallei (*B. pseudomallei*) is the pathogen of fatal tropical infectious disease melioidosis. This study screened sRNA BprsO from extracellular vesicles (EVs) of *B. pseudomallei* as a new biomarker and constructed a lateral flow strip assay (LFSA) with dual signal amplification for its visual biosensing by coupling catalytic hairpin assembly (CHA) with MXene@PtCu nanozymes. The platinum nanoparticles (Pt NPs) in the nanozymes provided a large number of active sites for the assembly of nucleic acid and antibodies, and enhanced the catalytic activity of Cu NPs through their synergistic effect. The large specific surface area of MXene avoided the aggregation of Pt and Cu NPs for improving the signal output. Moreover, CHA technology not only recycled the target, but also successfully introduced biotin-labeled probes to the nanozymes surface, ultimately converting the nucleic acid concentration into easily accessible visual detection signals. Benefiting from the twofold amplification of MXene@PtCu and CHA, the proposed colorimetric assay exhibited superior performance for BprsO detection with a dynamic range from 50 aM to 5 nM, and a detection limit of 5 aM. Notably, the method was successfully implemented in the context of LFSA, thereby illustrating its capacity for the visual detection of BprsO at a concentration as low as 15 fM and achieving a detection sensitivity of 1.26 fM. This work validates that the screened BprsO can serve as a specific biomarker for *B. pseudomallei*, and proposes a strategy with high sensitivity and specificity that offers a robust visual platform for early diagnosis and monitoring of *B. pseudomallei*.

1. Introduction

Burkholderia pseudomallei (*B. pseudomallei*) is a causative agent of melioidosis in both humans and animals [1]. Melioidosis manifests with various clinical symptoms, a high mortality rate (40 %), and a prolonged incubation period, posing challenges for early diagnosis [2,3]. Current detection techniques include conventional culture methods [4], polymerase chain reactions (PCR) based on bacterial nucleic acids [5–10], antibodies detection in serum by enzyme linked immunosorbent assay (ELISA) [11]. However, these methods are generally expensive, labor-intensive, and time-consuming, requiring complicated genome amplification processes, strict primer design, verification of antibody specificity, yet still exhibit low sensitivity in the early stage of infection [12–14]. Therefore, it is of utmost importance to identify a new specific biomarker that can be effortlessly detected in body fluids during the early stages of infection, as well as to devise a rapid, accurate, and ultra-sensitive diagnostic strategy.

As a widespread biomarker both in cells and bacteria, extracellular vesicles (EVs) have provided powerful tools for early disease diagnosis, prognosis, dynamic monitoring, etc. [15] in recent years. EVs in body fluids can indicate corresponding changes according to the development of the disease, which can accurately reflect the pathological state in the body and its evolution process [16,17]. Moreover, EVs have obvious advantages such as non-invasive, easy sampling and real-time

* Corresponding authors.
E-mail addresses: diaoqizhi@163.com (Q. Diao), hxju@nju.edu.cn (H. Ju), xiaqianfeng@hainmc.edu.cn (Q. Xia).
[1] These authors contributed equally to this work.

https://doi.org/10.1016/j.snb.2024.137195
Received 26 November 2024; Received in revised form 23 December 2024; Accepted 25 December 2024
Available online 26 December 2024

monitoring [18]. It contains a variety of bioactive substances, including proteins, lipids, and nucleic acids [19]. Among them, sRNAs are protected from RNase degradation in the external environment, making them an ideal target for diagnostic biomarker development [20,21]. However, its small size, low abundance, and high sequence similarity of the sRNA family pose specific challenges to traditional RNA detection techniques [22–24]. Therefore, it is necessary to search for new diagnostic biomarkers from EVs of *B. pseudomallei* and construct accurate and sensitive point-of-care testing (POCT) methods to improve the efficiency of early diagnosis of melioidosis, especially in resource-limited

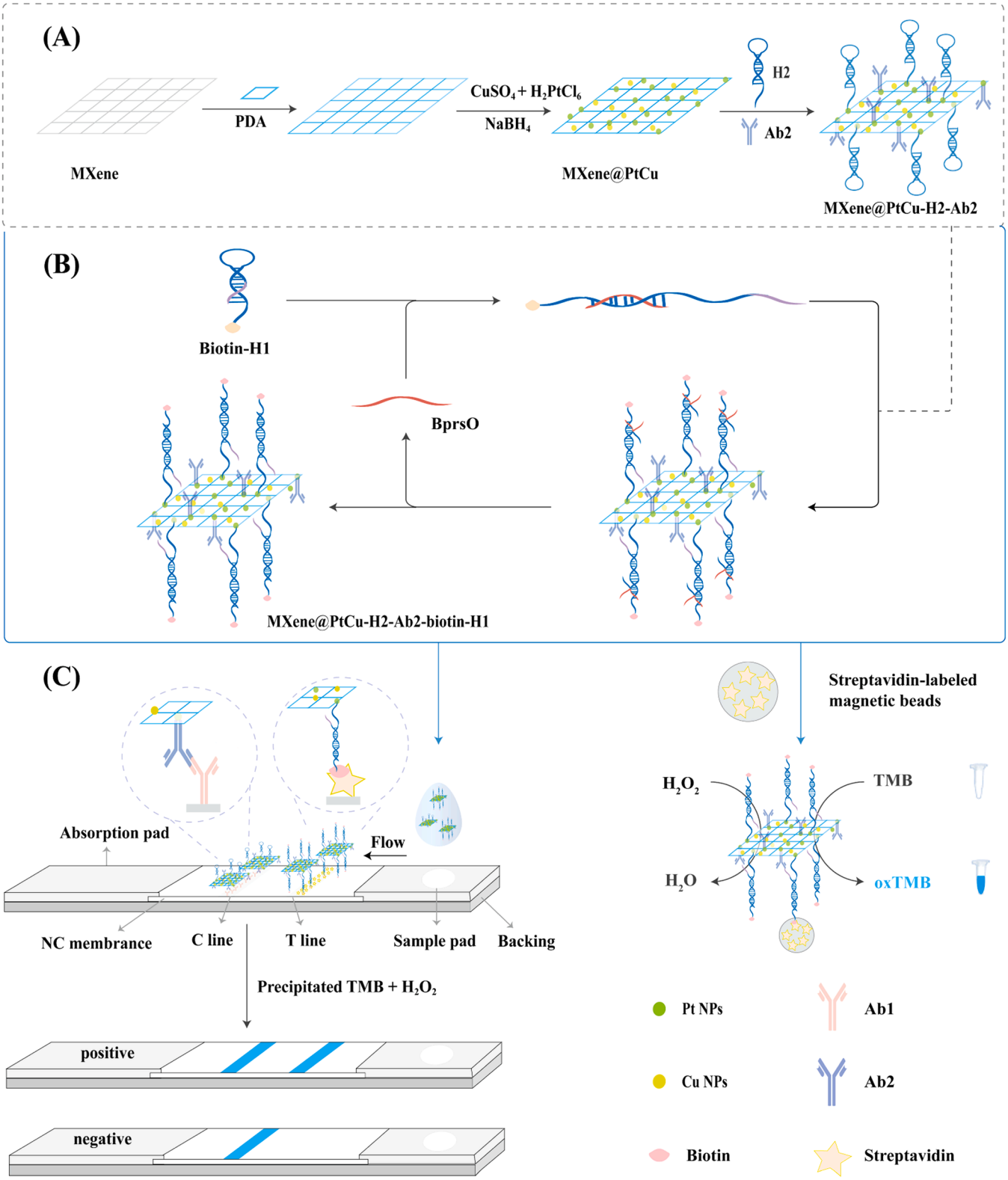

Scheme 1. Schematic illustration of POCT biosensor. (A) Preparation of MXene@PtCu nanozymes; (B) MXene@PtCu-based biosensor for the detection of BprsO; (C) the principle of paper based LFSA and colorimetric assay.

environments.

As representatives of POCT diagnostic methods, colorimetric assays and lateral flow assays (LFA) offer the advantage of direct result interpretation [24]. The simplicity of operation, portability, and cost-effectiveness of above methods make them suitable for disease diagnosis, environmental monitoring, and food safety in resource-limited locations [25,26]. Nucleic acid based POCT biosensors have been developed for the detection of circulating tumor cells [27], extracellular vesicles [28], pesticide content on food surfaces [29], and enzyme activity [30]. However, the limited sensitivity restricts their practical application. Moreover, catalytic hairpin assembly (CHA), a promising enzyme-free isothermal amplification technology, has shown high potential for POCT application due to its rapid and efficient amplification, minimal background, and rapid target turnover [31].

In addition to efficient amplification of CHA biometric events, efficient signal output is a key indicator for the development of ultrasensitive biosensors [32]. Nanozymes, nanomaterials with enzyme-like catalytic activity, typically consisting of metal NPs, especially bimetallic NPs [33], have garnered significant interest in biosensor signal amplification [34]. Nevertheless, due to their high surface energy and the possible agglomeration and deactivation that can occur during the preparation and catalytic reactions, the catalytic activity and selectivity of nanozymes are significantly affected [35,36]. To overcome this issue, two-dimensional (2D) nanomaterials like graphene, metal-organic frameworks, and metal oxides are frequently employed to immobilize metal NPs [37,38]. As a 2D transition metal carbonitride, MXene often serves as an ideal material for signal amplification and demonstrates significant potential in biosensor construction, due to its large surface area, abundant surface functional groups and excellent hydrophilicity [39]. When used as a supporting material for metal NPs, MXene not only enhances the stability and dispersion of the NPs, but also exhibits a robust interaction between the composite material components (such as metal and carrier, metal and metal) [40,41]. Based on this design, the catalytic activity and selectivity of the nanozymes were significantly improved [42].

Due to the absence of simple and specific diagnostic biomarkers, the challenges confronted by the diagnostic approaches for melioidosis, and the significance of EVs content in diagnosis. In this article, RNA extraction and sequencing, target gene function prediction, and sequence-specific analysis were conducted on *B. pseudomallei* EVs to screen for new diagnostic sRNA markers of melioidodsis. Based on these analyses, a highly sequence-specific sRNA, named BprsO, had been identified as a potential biomarker for the detection of *B. pseudomallei*. To achieve rapid, sensitive and visual detection of BprsO, a dual-signal amplification strategy was developed by integrating CHA and MXene@PtCu nanozymes.

In the designed biosensor, MXene was initially encapsulated with polydopamine (PDA) to prevent surface oxidation reactions and ensure nanoparticle dispersion. Subsequently, Pt and Cu NPs were deposited in situ on MXene to synthesize nanozymes, MXnen@PtCu. Furthermore, Pt NPs offered more binding sites for the modification of hairpin probe 2 (H2) and Ab2 on the nanozymes (Scheme 1A). In the presence of BprsO, the biotin-labeled H1 molecule was opened, which subsequently led to the activation of H2. The energy barrier associated with base pairing facilitated the displacement of BprsO by H2, which achieved the recycling of target sequences and successfully introduces biotin labeled H1 onto the nanozymes. This process resulted in the formation of a significant number of double-stranded assemblies (Scheme 1B). These assemblies were captured by streptavidin on the test line (T-line), whereas the assemblies that did not undergo the CHA reaction were captured by Ab1 on the control line (C-line). The corresponding positions exhibited significant colorimetric reactions on the LFSA, catalyzed by the nanozyme in the conversion of TMB, ultimately enabling the visual detection of BprsO (Scheme 1C). This innovative design offers robust signal support for biosensing, further enhancing detection sensitivity and accuracy.

2. Experimental section

Due to the word limit, experimental sections have been put in the supplementary materials.

3. Results and discussion

3.1. Characterization of MXene@PtCu

To characterize the size and morphology of MXene@PtCu, Transmission Electron Microscope (TEM) and High-Angle Annular Dark Field (HADDF) techniques were performed. As reported in the literature [27], MXene exhibited a 2-D sheet structure (Fig. 1A). The roughly spherical NPs exhibited uniformly deposition on MXene nanosheets (Fig. 1B). Two NPs with different lattice fringe spacings (0.23 nm and 0.21 nm) were observed, corresponding to the d-spacing in the planes of Pt NPs (111) and Cu NPs (111), respectively (Fig. 1C) [43,44]. The characteristic lattice confirmed the successful synthesis of Pt NPs and Cu NPs within 2-D MXene. Particle size analysis revealed that the particle sizes of Pt and Cu NPs were (2.9 ± 0.9) nm and (5.1 ± 1.5) nm (Fig. S1), respectively. This size was optimal for achieving high catalytic activity of Pt NPs [45,46]. Additionally, the result of element distribution of MXene@PtCu showed that the Pt and Cu elements were evenly distributed on 2-D MXene (Fig. 1D-I). Further evidence from X-ray photoelectron spectroscopy (XPS) revealed that this heterostructure was composed of C, Ti, Cu, and Pt (Fig. 1J). Peaks centered at 931.87 eV and 951.83 eV were attributed to Cu 2p, corresponding to metallic Cu $2p_{3/2}$ and Cu $2p_{1/2}$ bands(Fig. 1K), respectively. These peaks displayed binding energy differences of atoms to the outermost electrons compared to the standard Cu^0 (Cu $2p_{3/2}$ at 932.7 eV and Cu $2p_{1/2}$ at 952.56 eV) [47], The Pt 4 f spectrum exhibited two distinct peaks at 71.35 eV (Pt 4 $f_{7/2}$) and 74.66 eV (Pt 4 $f_{5/2}$) (Fig. 1L), which were positively shifted compared to the binding energies of standard metallic Pt^0 (71.2 eV and 74.4 eV) [48]. This result suggested that the doping of Cu NPs results in alterations to the distribution of electrons on the surface of Pt NPs, which expedited the transfer of electrons beyond the nucleus, thereby influencing the catalytic activity of nanomaterials.

3.2. Catalytic activity of MXene@PtCu

Typical 3,3′,5,5′-Tetramethylbenzidine (TMB) oxidation reaction was conducted to investigate the peroxidase activity of MXene@PtCu. As shown in Fig. 2A, there was no characteristic absorption peak at 652 nm observed in the presence of MXene and MXene@Cu (curves ii, iii), which suggested that MXene and MXene@Cu has no catalytic activity. However, upon the addition of MXene@Pt, an increased absorbance was observed (curve iv) compared to curves ii, iii. Surprisingly, the addition of MXene@PtCu resulted in a significant absorbance enhancement (curve v) compared to MXene@Pt. The inset image illustrated the corresponding color changes. The results above indicated that Pt NPs played the primary catalytic role in nanozymes, and the introduction of Cu NPs enhanced catalytic activity, which might be attributed to the neighboring metal atoms in binuclear metal catalysts, exerting a synergistic effect to reduce the free energy barrier in the transition state [49]. In Fig. 2B, the absorbance slope of MXene@PtCu (curve g) was higher than that of Pt NPs (curve b) and PtCu NPs (curve c), yet slightly lower than that of HRP (curve h). This suggested that MXene@PtCu exhibited catalytic activity comparable to HRP.

The generation of reactive oxygen species (ROS) within the catalytic system was found to be intimately linked to the catalytic activity. As illustrated in Fig. 2C-D, the Electron Paramagnetic Resonance (EPR) spectrum displayed characteristic peaks corresponding to the DMPO-OH adduct, with an intensity ratio of 1:2:2:1, in conjunction with the distinct peaks associated with the DMPO-$O_2^{\bullet-}$ adduct. In comparison to the pristine MXene material, the composites MXene@Cu, MXene@Pt, and MXene@PtCu all exhibited two prominent peaks, suggesting their

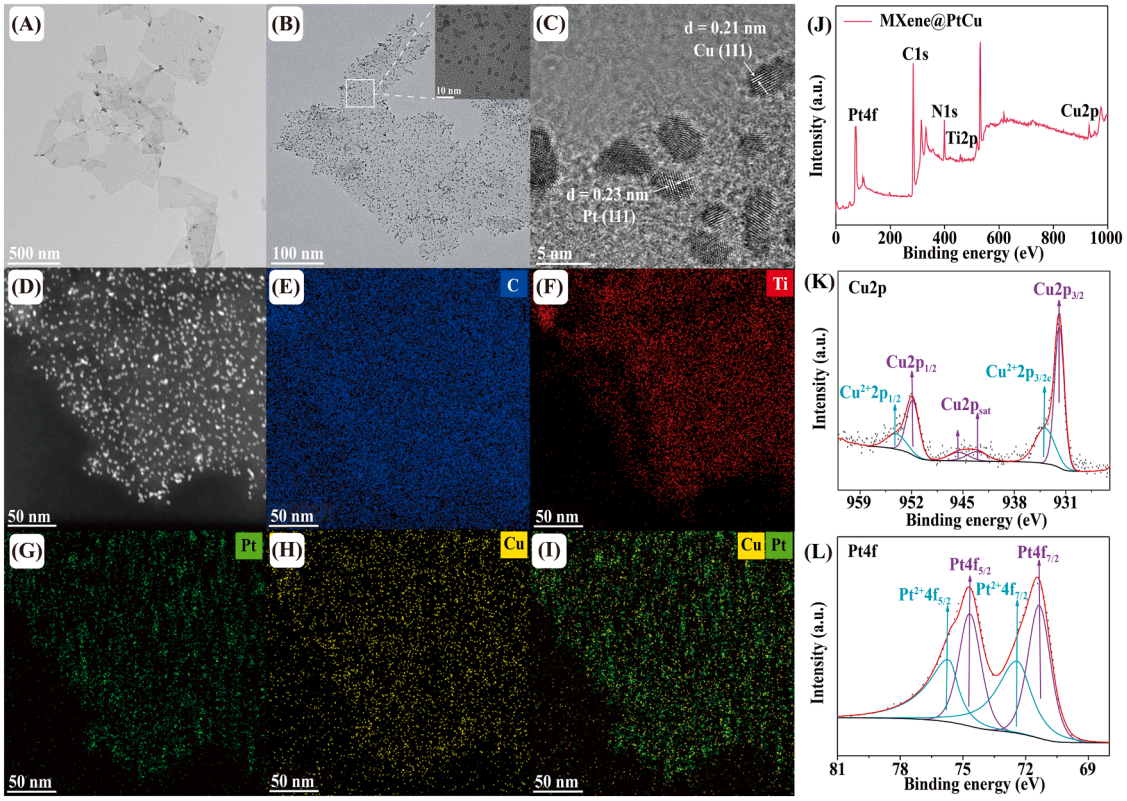

Fig. 1. TEM image of (A) MXene, (B) MXene@PtCu, inset showing TEM image of NPs shape. (C) HR-TEM image of MXene@PtCu. (D) HAADF image of MXene@PtCu. Elemental mapping images of (E) C, (F)Ti, (G) Pt,and (H) Cu, and (I) PtCu in MXene@PtCu. (J) XPS survey spectra of MXene@PtCu composites. High-resolution XPS of (K) Cu 2p and (L) Pt 4 f.

ability to catalyze the decomposition of hydrogen peroxide into hydroxyl radicals (OH•) and superoxide radicals ($O_2^{\bullet-}$). Notably, the MXene@Cu composite generated significantly lower levels of ROS, which were nearly negligible when compared to those produced by MXene@Pt. The minimal quantity of ROS was not sufficient to elicit a direct color change in TMB, resulting in the absence of the characteristic peak of oxidized TMB oxTMB at 652 nm (Fig. 2A, curve iii). Following the synthesis of the MXene@PtCu nanozyme, a substantial increase in ROS production was observed. This observation was consistent with the experimental results obtained from the catalysis of TMB, further substantiating that the incorporation of Cu NPs significantly enhanced the catalytic efficiency of the MXene@PtCu composite. This outcome also lent support to the hypothesis that Cu NPs induced alterations in the electronic structure of Pt NPs.

The catalytic mechanism of nanozymes was illustrated in Fig. 2E. Pt NPs and Cu NPs catalyzed the generation of HO• and $O_2^{\bullet-}$ from hydrogen peroxide; HO• could further react with HO_2^-, producing $O_2^{\bullet-}$ [10]. Subsequently, the generated $O_2^{\bullet-}$ react with TMB, producing the blue oxTMB. Compared to individual components, the synergistic catalysis of MXene@PtCu significantly enhances the production of $O_2^{\bullet-}$. Additionally, TMB could adsorb Pt NPs and Cu NPs on the surfaces, reducing the transmission distance of $O_2^{\bullet-}$ and enhancing their catalytic capability towards TMB [50]. The results indicated that MXene@PtCu, with synergistic and proximity catalytic characteristics, could serve as a biosensor probe, significantly improving detection sensitivity.

To ensure the accuracy and repeatability of detection outcomes, we conducted a comprehensive assessment the pH-, thermal-, and buffer-stability of MXene@PtCu. As depicted in Fig. 2F, after six days of storage, the relative standard deviation (RSD) for the catalytic activity of the nanozyme remained below 5 % across various pH solutions, suggesting that the storage duration has a minimal effect on the catalytic performance of MXene@PtCu. Notably, as the pH increased, the catalytic activity also rose, which indicating that the catalytic efficiency was positively correlated with pH elevation. The catalytic activity remained above 93.87 % within a temperature range of 30–60°C and still retained 83.68 % at 90°C, signifying those different temperatures exerted minimal influence on the material's catalytic activity (Fig. 2G). Cu NPs could easily react with water or ions in buffers to etch out due to corrosion. In comparison with HEPES and Tris-HCl, the material displayed the minimal impact in phosphate-buffered saline (PBS), with a RSD of 2.6 %, and retained 89.91 % of its activity (Fig. 2H). In conclusion, the exceptional stability of MXene@PtCu with respect to pH, thermal conditions, and buffer solutions qualified it as an ideal multifunctional probe for enhancing the detection capabilities of sensors.

3.3. Feasibility assessment of colorimetric assay

EVs were isolated from *B. pseudomallei* culture medium (Fig. S2), and RNA sequencing was performed. The results revealed that EVs contained 85 known sRNA sequences and 15 previously unrecognized sRNA sequences, both playing critical roles in bacterial biological activities and disease therapeutic mechanisms (Fig. S3A). Further analysis indicated that BprsO was closely associated with bacterial biofilm formation, drug metabolism, and flagellar generation, thereby regulating bacterial metabolism and quorum sensing (Fig. S3B). Sequence alignment on NCBI revealed that BprsO mainly existed in the genus *Burkholderia* with high specificity in *B. pseudomallei* (83 %) (Fig. S3C). Therefore, BprsO could serve as a potential novel biomarker for detection of *B. pseudomallei* infection.

12 % PAGE was employed to visually reveal the CHA reaction process. As shown in Fig. 3A, compared with L1 and L3, L4 displayed distinct and uniform bands with lower mobility. It was indicated that the hairpin probe H1 could only be opened under the presence of BprsO. L5 showed a clear band with lower mobility compared to L1, L2 and L4,

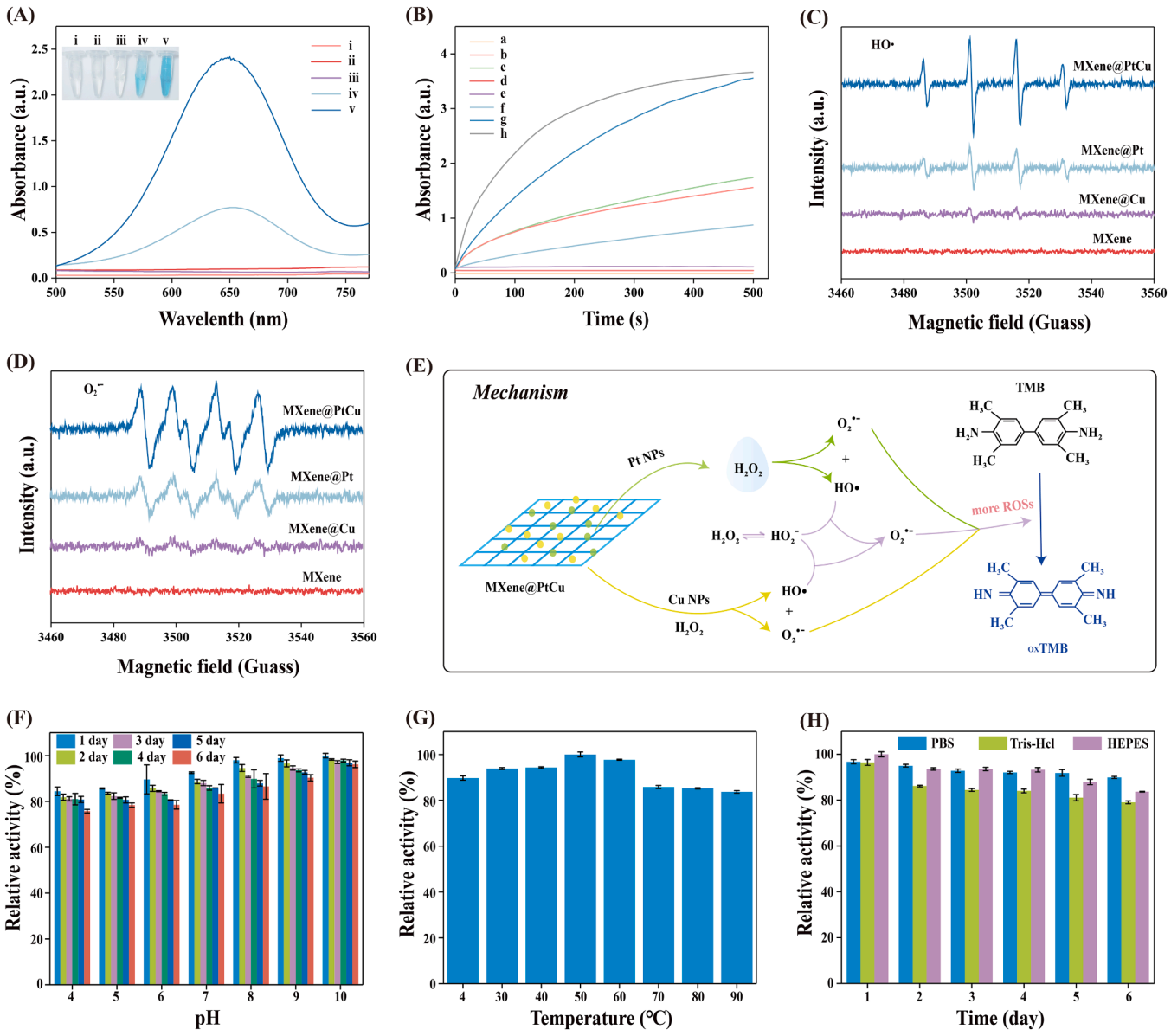

Fig. 2. Investigation of the catalytic activity of the nanozymes. (A) UV–vis absorption spectra of different reaction system: (i) H_2O_2 + TMB, (ii) H_2O_2 + TMB + MXene, (iii) H_2O_2 + TMB + MXene@Cu, (iv) H_2O_2 + TMB + MXene@Pt, (v) H_2O_2 + TMB + MXene@PtCu; insets showing color images. (B) Time-dependent absorbance: (a) H_2O_2 + TMB, (b) H_2O_2 + TMB + Pt, (c) H_2O_2 + TMB + PtCu, (d) H_2O_2 + TMB + MXene, (e) H_2O_2 + TMB + MXene@Cu, (f) H_2O_2 + TMB + MXene@Pt, (g) H_2O_2 + TMB + MXene@PtCu, (h) H_2O_2 + TMB + HRP. EPR spectra of (C) DMPO-OH adducts and (D) DMPO-$O_2^{\bullet-}$ adducts in the different systems. (E) Diagram of the possible MXene@PtCu catalytic mechanism. Relative activity of MXene@PtCu for oxidizing TMB under varying conditions: (F) pH, (G) temperature, and (H) buffer solutions.

indicating that the free end of H1 opened by BprsO could further open the H2 hairpin. Due to the difference in energy between chains during binding, H2 would occupy the binding site between the BprsO and H1, thereby replacing BprsO from H1 and ultimately accomplishing BprsO recycle. These results indicated that CHA could only proceed in the presence of target sequence.

The Zeta potential measurements corroborate the surface modification of MXene (Fig. 3B), demonstrating that the cationic polymer PDA successfully coats the surface, leading to an increase in the Zeta potential from −27.70 mV to −9.24 mV. Upon the loading of PtCu NPs, the Zeta potential subsequently increased to −3.84 mV. Given that both DNA and proteins carry negative charges, following the sequential modification of MXene@PtCu with h2 and Ab2, there was a progressive decrease in the Zeta potential from −3.84 mV to −5.87 mV, and subsequently to −8.81 mV. These findings suggested that both H2 and Ab2 had been effectively conjugated to the surface of the nanozyme. Similarly, the Zeta potential of SMB was found to be −5.84 mV, indicating the presence of electrostatic repulsion between SMB and MXene@PtCu-H2-Ab2, which effectively prevented non-specific adsorption of MXene@PtCu-H2-Ab2 onto the SMB surface. Fourier-transform infrared (FT-IR) spectra analysis was conducted to further verify the functionalization of MXene@PtCu (Fig. S4). The thiol group (- SH) was modified at the 3′-end of H2, and this functional group exhibited a distinct characteristic peak at 2605 cm^{-1}. Pt was covalently bonded to DNA through Pt-S bonds [51]. Thus, when H2 and MXene@PtCu was connected through Pt-S bonds, a clear characteristic peak of thiol groups appeared at 2605 cm^{-1}, indicating successful H2 modification on the MXene@PtCu nanozymes.

Electrochemical impedance spectroscopy (EIS) was used to confirm the layer-by-layer modification on the GE using the electroactive probes

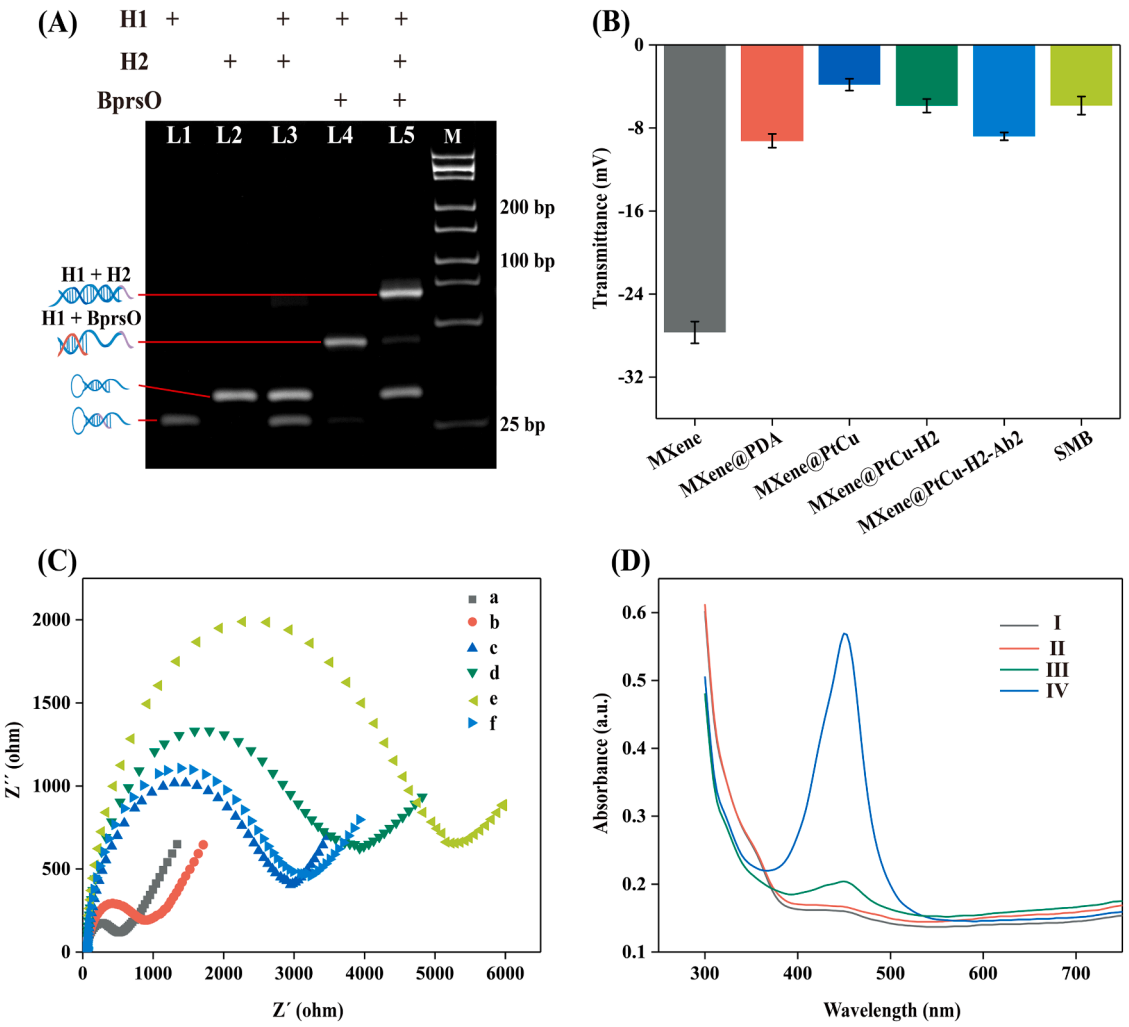

Fig. 3. Evaluation of the feasibility of colorimetric assay. (A) PAGE image. (B) Zeta potential of MXene, MXene@PDA, MXene@PtCu, MXene@PtCu-H2, MXene@PtCu-H2-Ab2 and SMB. (C) EIS profiles of (a) bare GE, (b) streptavidin / GE, (c) BSA / streptavidin / GE, (d) biotin-H1 / BSA / streptavidin / GE, (e) BprsO / biotin-H1 / BSA / streptavidin / GE, and (f) MXene@PtCu-H2-Ab2 / BprsO / biotin-H1 / BSA / streptavidin / GE in 5.0 mmol/L $[Fe(CN)_6]^{-3/-4}$ and 0.1 mol/L KCL. (D) UV–vis absorption spectra of (I) SMB, (II) MXene@PtCu-H2-Ab2 / SMB, (III) biotin-H1 / MXene@PtCu-H2-Ab2 / SMB, and (IV) BprsO / biotin-H1 / MXene@PtCu-H2-Ab2 / SMB. Error bar represents Standard Deviation (SD, n = 3).

$[Fe(CN)_6]^{4-/3-}$. As shown in Fig. 3C, after immobilizing streptavidin on the GE surface, a larger electron-transfer resistance (R_{et}) was observed compared to the bare GE. With BSA addition the R_{et} further increased due to BSA hindering electron transfer. Subsequently, upon the addition of biotin-H1 and the target, the R_{et} increased again. However, when MXene@PtCu-H2-Ab2 was incubated on the modified GE, a significantly reduced R_{et} was observed (Curve g), attributed to the excellent conductivity of MXene@PtCu. The results indicated that in the presence of the target sequence, MXene@PtCu-H2-Ab2 successfully combined with H1 through complementary base pairing. The feasibility of colorimetric assay was further investigated using UV–vis absorption spectra. In Fig. 3D, The absence of discernible absorption peaks in both Curve I and Curve II provided compelling evidence for the lack of non-specific interaction between the nanozyme and SMB. Compared to curves I-III, a clear UV absorption peak at 450 nm was detected in the presence of BprsO. These results robustly confirmed the feasibility of the proposed biosensor.

3.4. Optimization of detection conditions

To achieve excellent analytical performance, key parameters of colorimetric assay, including the ratio of H1 to H2 (H1: H2), CHA reaction time, streptavidin-labeled magnetic beads (SMB) concentration, and SMB reaction time, were optimized. Under the conditions of a CHA reaction time of 60 minutes, an SMB concentration of 2 mg mL^{-1}, and an SMB reaction time of 25 minutes, the ratio of H1 to H2 was determined. In Fig. S5A, as the H1: H2 ratio decreased, the positive signal gradually increased until reaching a plateau at H1: H2 = 1:1, with no significant change in the background group, and the signal-to-background ratio (S/B) was highest at H1: H2 = 1:1. This might be attributed to the fact that the fixed concentration of H1 has been fully utilized. Consequently, the H1:H2 ratio of 1:1 was chosen as the optimal probe ratio for all subsequent experiments. With all other parameters held constant, the signal intensity progressively increased with the extension of the CHA reaction time; nonetheless, a notable increase in background signal was observed when the reaction time surpassed 60 minutes. The maximum S/B was achieved at a reaction time of 60 minutes (Fig. S5B). The signal gradually increased with the rising concentration of SMB, reaching a plateau at 3 mg mL^{-1}. However, further increased in SMB concentration led to an elevated background, resulting in a significantly lower S/B (Fig. S5C). This might be attributed to excessive nonspecific adsorption on the SMB surface, eventually resulting in an increased background. In Fig. S5D, the binding time of CHA product and SMB was optimized, with the optimal binding time

determined to be 25 minutes.

Based on the experimental verification above, the optimal experiment parameters were: a 1:1 concentration ratio of H1 and H2, 60-minute CHA reaction time, SMB concentration at 3 mg mL^{-1}, and 25-minute binding time for the CHA products and SMB.

3.5. Analytical performance of colorimetric assay

The biosensor's sensitivity was investigated under optimal experimental conditions by adjusting the concentration of BprsO. In Fig. 4A, as the concentration of BprsO increased, the absorbance also increased. The ΔA (ΔA=A_{BprsO}-A_0, A_0: absorbance without BprsO) showed a robust linear relationship with the logarithm (lg) of corresponding target concentrations, ranging from 0 to 5 nM ($\Delta A = 0.0224 \times \lg C_{BprsO} + 0.0422$, $R^2 = 0.9953$, and C: the concentration of BprsO, Fig. 4B). Concentration of target BprsO as low as 5 aM could be detected, with a distinct increase in the absorption spectrum compared to the negative control curve. In other words, the designed method was able to detect several-copies synthetic target in the 10 μL reaction system, revealing higher sensitivity than reported RNA assays (Table S2). We had reported several effective methods for *B. pseudomallei* detection, including ratiometric fluorescence biosensor based on energy transfer, electrochemistry, ECL, and LFSA based on PCR (Table S3). However, despite achieving sensitive detection, these methods targeted bacterial DNA or PCR amplification products and required complex operation, expensive instruments and professional technical personnel, which limited their clinical translation. Compared to previous *B. pseudomallei* DNA detection methods, the biosensor developed in this work directly detects EV-sRNA. It offers simple operation, portability, normal temperature application, and results readable by the naked eye. Additionally, it provides high sensitivity and a wide detection range without needing sophisticated equipment or stringent lab conditions. This relied on signal amplification from the target cycle of CHA and secondary enhancement from the high peroxidase activity of nanozymes.

Single-base mismatch (SBM), double-base mismatch (DBM), triple-base mismatch (TBM), and known *B. pseudomallei* sRNAs (sRNA-11614, sRNA-1579, sRNA-4562, sRNA-5324, and sRNA-638) were used to assess the specificity of our biosensor. In Fig. 4C, compared with other sRNA, the detection system was able to produce a significant absorbance only when BprsO was present, indicating a high recognition ability for BprsO in this colorimetric assay. This primarily relied on the specific recognition and opening of hairpin probe H1 by BprsO.

Additionally, a recovery experiment was performed by introducing different concentrations of BprsO into diluted human serum samples. As shown in Table 1, the recovery rates ranged between 97.04 % and 104.39 %, and the relative RSD ranged from 4.74 % to 7.40 %. These results fully confirmed the reliability and practical application potential of the proposed strategy.

Table 1
The recovery experiment of colorimetric assay using synthetic BprsO strands piked serum sample.

Added (aM)	Detected I (aM)	Detected II (aM)	Detected III (aM)	Recovery (%)	RSD (%)
1.0×10^3	1.11×10^3	1.06×10^3	0.96×10^3	104.39	7.40
1.0×10^5	0.98×10^5	1.01×10^5	1.08×10^5	102.52	5.32
1.0×10^8	0.96×10^8	0.93×10^8	1.02×10^8	97.04	4.74

3.6. Feasibility and analytical performance of LFSA

LFSA was performed to achieve convenient on-site detection without instrument and improve signal readout convenience. As shown in Fig. 5A, two bright blue lines appeared on the test strip in the presence of the target; whereas without target, the test strip showed solely one bright blue C line. These results confirmed the successful detection of BprsO by LFSA.

To improve the detection performance of the developed LFSA, the experimental conditions was optimized. This optimization process involved adjusting the concentrations of MXene@PtCu and streptavidin on the T-line, as well as the reaction and coloration times for the test strips (Fig. S6). Under optimal conditions, the test strips were utilized for the detection of BprsO within the concentration range of 0–1.5 nM. The color intensity of the T-line increased progressively with the increasing concentrations of BprsO. Notably, a distinct blue band was clearly visible on the T-line at a concentration as low as 15 fM. However, at a concentration of 1.5 fM, the T-line was imperceptible, signifying a visual limit of detection (vLOD) of 15 fM for the LFSA (Fig. 5B). By plotting the optical density values of the T-line against BprsO concentrations, a calibration curve was obtained ($I = 2221.8965 \times \lg C_{BprsO} + 10204.8565$, $R^2 = 0.9841$, I: the intensity of T-line, and C: the concentration of BprsO, Fig. 5C). The LOD, defined as the average optical density of blank samples plus three times the SD, was determined to be 1.26 fM. The proposed LFSA exhibited ultra-high sensitivity and a broad linear range. The high sensitivity was attributed to the high catalytic activity of MXene@PtCu nanozymes and the efficient chain replacement capacity of CHA.

The following test utilized serum samples that were free of BprsO as the negative control, and those that included BprsO (0.2 pM) as the positive control. The LFSA results for various known sRNA originating from *B. pseudomallei* and BprsO mutants demonstrated that the blue band on the T-line was exclusively observed in the presence of BprsO (Fig. 5D). The corresponding T-line intensities also demonstrated a

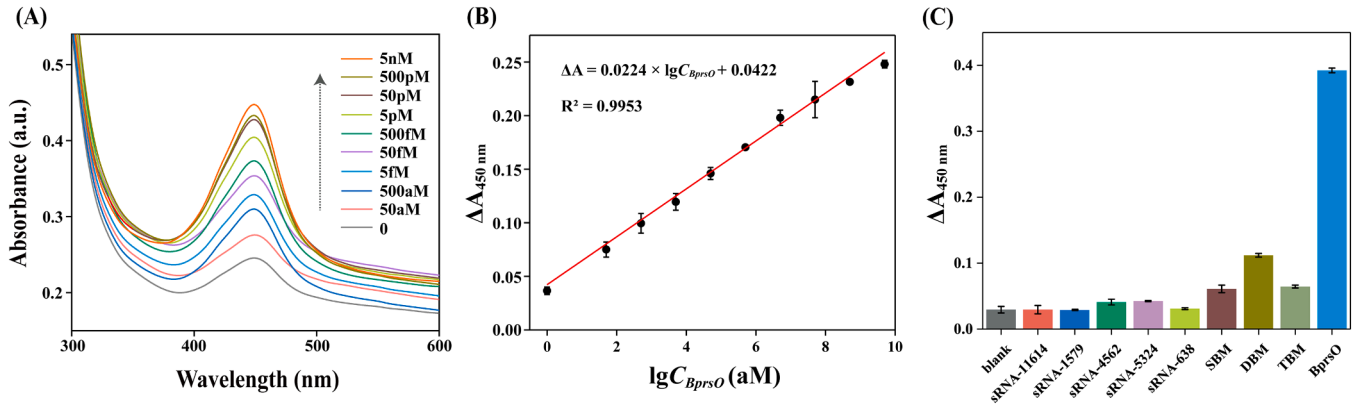

Fig. 4. Analytical performance of colorimetric assay. (A) UV–vis absorption spectra of different BprsO concentrations ranging from 50 aM-5 nM. (B) The linear relationship of ΔA vs $\lg C_{BprsO}$. (C) Investigation of the specificity of the colorimetric assay by comparing absorbance to different sRNAs. Error bar represents SD (n = 3).

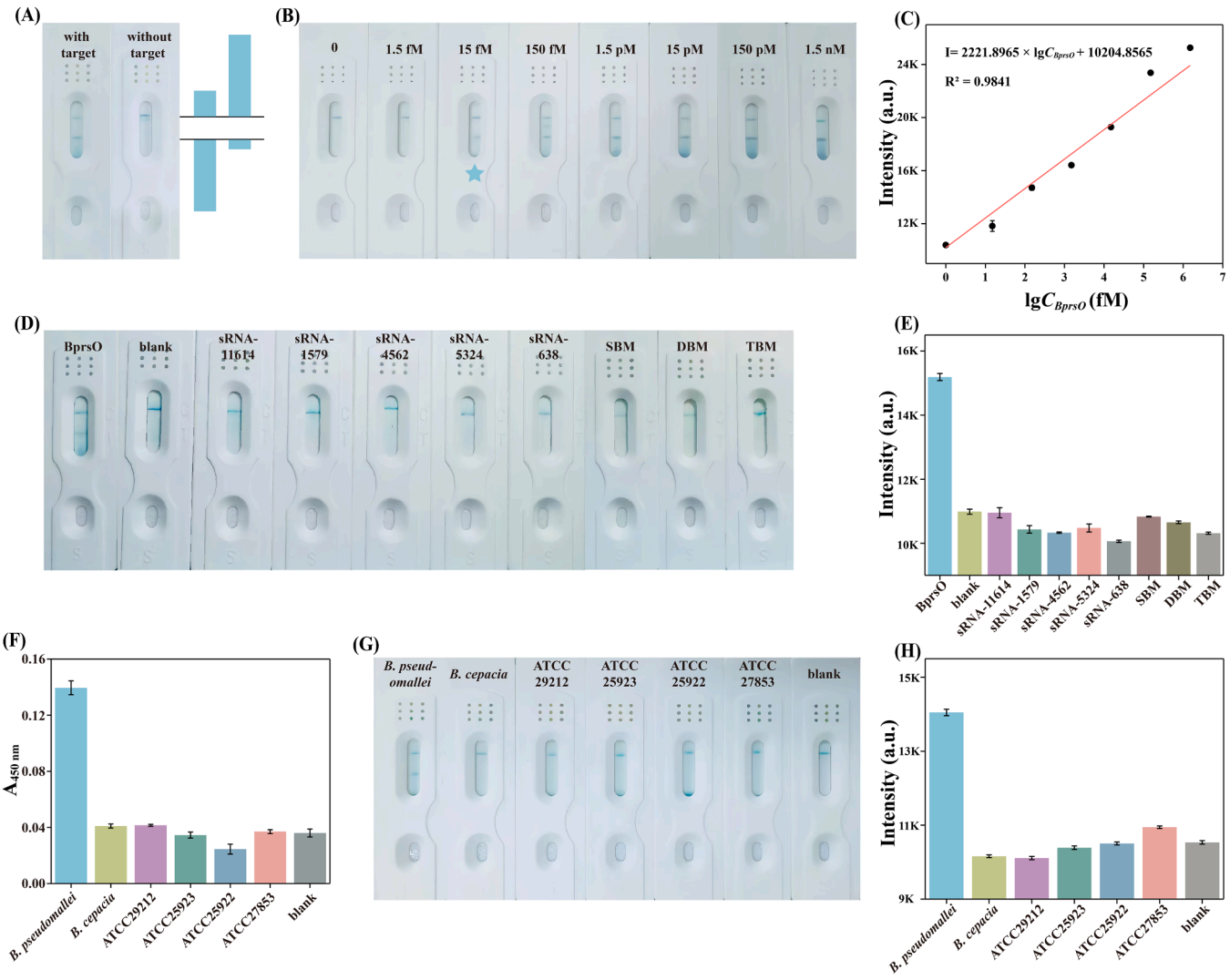

Fig. 5. (A) Feasibility of the LFSA. (B) Photographs of the test strips for detection BprsO at concentrations ranging from 0 to 1.5 nM. (C) Calibration curves of the T-line intensity. (D-E) Selectivity of test strip photographs and their corresponding T-line intensity, respectively. (F) Colorimetric assay, (G) test strip photographs and (H) their corresponding T-line intensity in the real samples analysis. Error bar represents SD (n = 3).

distinct signal response to BprsO (Fig. 5E). These finding underscored the high selectivity of the developed LFSA. To assess the repeatability of the LFSA, continuous monitoring of serum samples containing BprsO (0.75 pM) was conducted. The insignificant variations in optical density values on the T-line (RSD = 1.86 %, Fig. S7) suggested that the developed LFSA exhibited high repeatability.

To evaluate the accuracy and precision of the proposed LFSA, recovery experiments were performed utilizing serum samples with BprsO at concentrations of 0.03, 3, and 300 pM, respectively. The average recovery rates ranged from 95.90 % to 101.68 %, with RSD values between 2.60 % and 4.92 % (Table 2). These results indicated that the developed LFSA exhibited acceptable accuracy and precision for the quantification of BprsO in serum. Therefore, our new detection strategy had high sensitivity, specificity, and anti-interference capability, and was expected to be useful for the detection of *B. pseudomallei* EVs sRNA in clinical serum and environmental samples.

Table 2
The recovery experiment of LFSA using synthetic BprsO strands piked serum sample.

Added (fM)	Detected I (fM)	Detected II (fM)	Detected III (fM)	Recovery (%)	RSD (%)
3.0×10^1	2.93×10^1	2.77×10^3	3.05×10^3	97.23	4.92
3.0×10^3	3.16×10^3	2.97×10^3	3.01×10^3	101.68	3.27
3.0×10^5	2.82×10^5	2.96×10^5	2.85×10^5	95.90	2.60

3.7. Testing of the real samples

To further validate the practical application value of this strategy and the specificity of potential sRNA biomarker in *B. pseudomallei*, EVs RNA from *B. pseudomallei*, *B. cepacia* and four ATCC standard bacteria strains were extracted using Trizol. There is a significant absorbance difference between *B. pseudomallei* with other strains of bacteria (Fig. 5F). Only *B. pseudomallei* showed a band in the T-line of LFSA, while the reference strain of *B. cepacia* and four ATCC standard strains showed a band only in line C, all negative for T-lines (Fig. 5G). Fig. 5H revealed that the LFSA T-line intensity of *B. pseudomallei* was significantly distinct from those of other strains. These indicated that this new biomarker has good species specificity of *B. pseudomallei*. Compared to previous detection methods for *B. pseudomallei*, LFSA offers the advantages of no instrumentation, simple operation, and easy result interpretation.

4. Conclusion

In this study, a novel biomarker, BprsO, has been identified through analysis of EVs from *B. pseudomallei*. LFSA has been constructed by combining BprsO with a dual signal amplification strategy involving MXene@PtCu and CHA for simple, rapid, and ultra-sensitive visual detection of *B. pseudomallei*. Through the catalytic reaction of hydrogen peroxide, it was found that Pt NPs play a major catalytic role in MXene@PtCu. The addition of Cu NPs can enhance catalytic activity, due to synergistic catalytic effects between Pt NPs. The nanozymes' catalytic activity, comparable to HRP, and CHA's capability to cyclically target has been contributed to the biosensor with a broad linear range and high sensitivity. The chosen BprsO can act as a specific biomarker for diagnosing *B. pseudomallei*. Consequently, with high sensitivity, good specificity, convenient operation and acceptable recovery, the MXene@PtCu-based biosensor shows potential for the early diagnosis of melioidosis and holds promising prospects for clinical translation in visual detection. Future work will focus on implementing POCT in real clinical samples.

CRediT authorship contribution statement

Guozhen Tian: Data curation. **Hua Pei:** Data curation. **Qizhi Diao:** Writing – review & editing, Conceptualization. **Jun Tan:** Writing – original draft, Formal analysis, Data curation, Conceptualization. **Nini Luo:** Methodology, Formal analysis, Conceptualization. **Huangxian Ju:** Writing – review & editing, Methodology, Conceptualization. **Qianfeng Xia:** Writing – review & editing, Funding acquisition, Conceptualization. **Xuemiao Li:** Data curation. **Yanshuang Wang:** Data curation. **Ting Zhang:** Writing – review & editing, Conceptualization. **Juan Yao:** Methodology, Conceptualization.

Declaration of Competing Interest

The authors declare that they have no known competing financial interests or personal relationships that could have appeared to influence the work reported in this paper.

Acknowledgements

This research was supported by the National Natural Science Foundation of China (Grant Nos. 82370018 and 81960002), the Major Science and Technology Program of Hainan Province (ZDKJ202003, ZDKJ2021036), and State Key Research Development Program of China (2022YFC2305000, 2022YFC2305003).

Appendix A. Supporting information

Supplementary data associated with this article can be found in the online version at doi:10.1016/j.snb.2024.137195.

Data availability

Data will be made available on request.

References

[1] E.M. Meumann, D. Limmathurotsakul, S.J. Dunachie, W.J. Wiersinga, B.J. Currie, Burkholderia pseudomallei and melioidosis, Nat. Rev. Microbiol. 22 (2024) 155–169, https://doi.org/10.1038/s41579-023-00972-5.
[2] D. Limmathurotsakul, N. Golding, D.A.B. Dance, J.P. Messina, D.M. Pigott, C. L. Moyes, et al., Predicted global distribution of Burkholderia pseudomallei and burden of melioidosis, Nat. Microbiol. 1 (2016) 1–5, https://doi.org/10.1038/nmicrobiol.2015.8.
[3] Y. Wang, X. Li, D.A.B. Dance, H. Xia, C. Chen, N. Luo, et al., A novel lytic phage potentially effective for phage therapy against Burkholderia pseudomallei in the tropics, Infect. Dis. Poverty 11 (2022) 1–13, https://doi.org/10.1186/s40249-022-01012-9.
[4] P. Hemarajata, J.D. Baghdadi, R. Hoffman, R.M. Humphries, C.S. Kraft, Burkholderia pseudomallei: challenges for the clinical microbiology laboratory, J. Clin. Microbiol. 54 (2016) 2866–2873, https://doi.org/10.1128/jcm.01636-16.
[5] M.M. Win, T. Hla, K.P. Phyu, W.W. Aung, K.K. Nyein Win, S.N. Aye, et al., A study of Burkholderia pseudomallei in the environment of farms in Thanlyin and Hmawbi townships, Myanmar, Trans. R. Soc. Trop. Med. Hyg. 100 (2019) 1082–1084, https://doi.org/10.4269/ajtmh.18-0678.
[6] J. Yao, Z. Zhang, S. Tian, N. Luo, J. Tan, Y. Zhang, et al., Synchronous detection of Burkholderia pseudomallei and its ceftazidime resistance mutation based on RNase-HII hydrolysis combined with lateral flow strip assay, Microbiol. Spectr. 11 (2023) e01125-23, https://doi.org/10.1128/spectrum.01125-23.
[7] Y. Wang, B. Shen, N. Luo, C. Li, H. Wu, Y. Wang, et al., Self-enhanced nanohydrogel electrochemiluminescence biosensor based on CRISPR/Cas12a and gold platinum nanoparticles modification for high-sensitivity detection of Burkholderia pseudomallei, Chem. Eng. J. 486 (2024) 150279, https://doi.org/10.1016/j.cej.2024.150279.
[8] C. Li, C. Liu, R. Liu, Y. Wang, A. Li, S. Tian, et al., A novel CRISPR/Cas14a-based electrochemical biosensor for ultrasensitive detection of Burkholderia pseudomallei with PtPd@ PCN-224 nanoenzymes for signal amplification, Biosens. Bioelectron. 225 (2023) 115098, https://doi.org/10.1016/j.bios.2023.115098.
[9] S. Lin, Y. Lin, J. Wu, G. Li, X. Wu, N. Luo, et al., A ratiometric fluorescent biosensor for rapid detection of Burkholderia pseudomallei by dual CRISPR/Cas12a trans-cleavage assisted signal enhancement, Sens. Actuators B Chem. 379 (2023) 133204, https://doi.org/10.1016/j.snb.2022.133204.
[10] Y. Wang, R. Chen, B. Shen, C. Li, J. Chen, Y. Wang, et al., Electrochemiluminescent (ECL) biosensor for Burkholderia pseudomallei based on cobalt-doped MOF decorated with gold nanoparticles and N-(4-aminobutyl)-N-(ethylisoluminol), Microchim. Acta 189 (2022) 355, https://doi.org/10.1007/s00604-022-05402-6.
[11] P. Chaichana, K. Jenjaroen, P. Amornchai, S. Chumseng, S. Langla, P. Rongkard, et al., Antibodies in Melioidosis: the role of the indirect hemagglutination assay in evaluating patients and exposed populations, Am. J. Trop. Med. Hyg. 99 (2018) 1378–1385, https://doi.org/10.4269/ajtmh.17-0998.
[12] R. Velusamy, S. Muhi, Melioidosis and the heart: a systematic review, Trop. Med. Infect. Dis. 5 (2020) 121, https://doi.org/10.3390/tropicalmed5030121.
[13] M.N. Burtnick, P.J. Brett, V. Nair, J.M. Warawa, D.E. Woods, F.C. Gherardini, Burkholderia pseudomallei type III secretion system mutants exhibit delayed vacuolar escape phenotypes in RAW 264.7 murine macrophages, Infect. Immun. 76 (2008) 2991–3000, https://doi.org/10.1128/iai.00263-08.
[14] R.T. Novak, M.B. Glass, J.E. Gee, D. Gal, M.J. Mayo, B.J. Currie, et al., Development and evaluation of a real-time PCR assay targeting the Type III secretion system of Burkholderia pseudomallei, J. Clin. Microbiol. 44 (2006) 85–90, https://doi.org/10.1128/jcm.44.1.85-90.2006.
[15] S. Song, L. Zhu, C. Wang, Y. Yang, In vitro diagnostic technologies for the detection of extracellular vesicles: current status and future directions, View 4 (2023) 20220011, https://doi.org/10.1002/VIW.20220011.
[16] M. Tkach, C. Théry, Communication by extracellular vesicles: where we are and where we need to go, Cell 164 (2016) 1226–1232, https://doi.org/10.1016/j.cell.2016.01.043.
[17] Y. Jin, K. Chen, Z. Wang, Y. Wang, J. Liu, L. Lin, et al., DNA in serum extracellular vesicles is stable under different storage conditions, BMC Cancer 16 (2016) 753, https://doi.org/10.1186/s12885-016-2783-2.
[18] T. An, L. Zheng, Progress and analysis methods of clinical application of extracellular vesicle, J. South. Med. Univ. 37 (2017) 1559, https://doi.org/10.3969/j.issn.1673-4254.2017.11.23.
[19] J. Lee, O.Y. Kim, Y.S. Gho, Proteomic profiling of Gram-negative bacterial outer membrane vesicles: current perspectives, Proteom. Clin. Appl. 10 (2016) 897–909, https://doi.org/10.1002/prca.201600032.
[20] G. Lu, X. Jiang, A. Wu, J. Zhou, H. Liu, F. He, et al., Two small extracellular vesicle sRNAs derived from Mycobacterium tuberculosis serve as diagnostic biomarkers for active pulmonary tuberculosis, Front. Microbiol. 12 (2021) 642559, https://doi.org/10.3389/fmicb.2021.642559.
[21] L. Lv, C. Li, X. Zhang, N. Ding, T. Cao, X. Jia, et al., RNA profiling analysis of the serum exosomes derived from patients with active and latent Mycobacterium tuberculosis Infection, Front. Microbiol. 8 (2017) 1051, https://doi.org/10.3389/fmicb.2017.01051.
[22] Y. Fu, W. Li, Z. Wu, Y. Tao, X. Wang, J. Wei, et al., Detection of mycobacterial small RNA in the bacterial culture supernatant and plasma of patients with active tuberculosis, Biochem. Biophys. Res. Commun. 503 (2018) 490–494, https://doi.org/10.1016/j.bbrc.2018.04.165.
[23] A. Ebrahimi, H. Ravan, M. Mehrabani, Multiplex monitoring of Alzheimer associated miRNAs based on the modular logic circuit operation and doping of catalytic hairpin assembly, Biosens. Bioelectron. 170 (2020) 112710, https://doi.org/10.1016/j.bios.2020.112710.
[24] J. Peng, X. Hang, H. Wang, K. Zhao, H. Wang, H. Yu, et al., Low background self-primer EXPAR coupled with colorimetric and lateral flow assay for rapid and sensitive point-of-care detection of miRNA, Sens. Actuators B Chem. 399 (2024) 134856, https://doi.org/10.1016/j.snb.2023.134856.
[25] S. Liu, L. Dou, X. Yao, W. Zhang, B. Zhao, Z. Wang, et al., Polydopamine nanospheres as high-affinity signal tag towards lateral flow immunoassay for sensitive furazolidone detection, Food Chem. 315 (2020) 126310, https://doi.org/10.1016/j.foodchem.2020.126310.
[26] F. Di Nardo, M. Chiarello, S. Cavalera, C. Baggiani, L. Anfossi, Ten years of lateral flow immunoassay technique applications: trends, challenges and future perspectives, Sensors 21 (2021) 5185, https://doi.org/10.3390/s21155185.
[27] L. Yang, H. Guo, T. Hou, J. Zhang, F. Li, Metal-mediated Fe_3O_4@polydopamine-aptamer capture nanoprobe coupling multifunctional MXene@Au@Pt nanozyme

for direct and portable photothermal analysis of circulating breast cancer cells, Biosens. Bioelectron. 234 (2023) 115346, https://doi.org/10.1016/j.bios.2023.115346.
[28] X. Liu, X. Gao, L. Yang, Y. Zhao, F. Li, Metal-organic framework-functionalized paper-based electrochemical biosensor for ultrasensitive exosome assay, Anal. Chem. 93 (2021) 11792–11799, https://doi.org/10.1021/acs.analchem.1c02286.
[29] Y. Wang, Y. Wang, Y. Xue, X. Li, Y. Geng, J. Zhao, et al., Portable and flexible hydrogel sensor for on-site atrazine assay on agricultural products, Anal. Chem. 96 (2024) 7772–7779, https://doi.org/10.1021/acs.analchem.4c01579.
[30] X. Gao, X. Li, X. Sun, J. Zhang, Y. Zhao, X. Liu, et al., DNA tetrahedra-cross-linked hydrogel functionalized paper for onsite analysis of DNA methyltransferase activity using a personal glucose meter, Anal. Chem. 92 (2020) 4592–4599, https://doi.org/10.1021/acs.analchem.0c00018.
[31] H. Wu, M. Zou, X. Fan, F. Su, F. Xiao, M. Zhou, et al., Facile, rapid, and low-cost detection for Influenza viruses and Respiratory syncytial virus based on a catalytic DNA assembly circuit, ACS Omega 7 (2022) 15074–15081, https://doi.org/10.1021/acsomega.2c00882.
[32] G. Tian, W. Li, B. Liu, M. Xiao, Q. Xia, An enzyme-free electrochemical biosensor based on NiCoP@PtCu nanozyme and multi-MNAzyme junctions for ultrasensitive Uracil-DNA glycosylase detection, Sens. Actuators B Chem. 379 (2023) 133224, https://doi.org/10.1016/j.snb.2022.133224.
[33] X. Li, X. Li, D. Li, M. Zhao, H. Wu, B. Shen, et al., Electrochemical biosensor for ultrasensitive exosomal miRNA analysis by cascade primer exchange reaction and MOF@Pt@MOF nanozyme, Biosens. Bioelectron. 168 (2020) 112554, https://doi.org/10.1016/j.bios.2020.112554.
[34] Z. Wei, J. Sun, Y. Li, A.K. Datye, Y. Wang, Bimetallic catalysts for hydrogen generation, Chem. Soc. Rev. 41 (2012) 7994–8008, https://doi.org/10.1039/c2cs35201j.
[35] H. Li, J. Liao, Y. Du, T. You, W. Liao, L. Wen, Magnetic-field-induced deposition to fabricate multifunctional nanostructured Co, Ni, and CoNi alloy films as catalysts, ferromagnetic and superhydrophobic materials, Chem. Commun. 49 (2013) 1768, https://doi.org/10.1039/c3cc39237f.
[36] G.P. Sahoo, D. Kumar Bhui, D. Das, A. Misra, Synthesis of anisotropic gold nanoparticles and their catalytic activities of breaking azo bond in sudan-1, J. Mol. Liq. 198 (2014) 215–222, https://doi.org/10.1016/j.molliq.2014.06.032.
[37] J. Feng, Y. Li, M. Li, F. Li, J. Han, Y. Dong, et al., A novel sandwich-type electrochemical immunosensor for PSA detection based on PtCu bimetallic hybrid (2D/2D) rGO/g-C_3N_4, Biosens. Bioelectron. 91 (2017) 441–448, https://doi.org/10.1016/j.bios.2016.12.070.
[38] W. Yang, Q. Peng, Z. Guo, H. Wu, S. Ding, Y. Chen, et al., PtCo nanocubes/reduced graphene oxide hybrids and hybridization chain reaction-based dual amplified electrochemiluminescence immunosensing of antimyeloperoxidase, Biosens. Bioelectron. 142 (2019) 111548, https://doi.org/10.1016/j.bios.2019.111548.
[39] C. Liu, W. Yang, X. Min, D. Zhang, X. Fu, S. Ding, et al., An enzyme-free electrochemical immunosensor based on quaternary metallic/nonmetallic PdPtBP alloy mesoporous nanoparticles/MXene and conductive $CuCl_2$ nanowires for ultrasensitive assay of kidney injury molecule-1, Sens. Actuators B Chem. 334 (2021) 129585, https://doi.org/10.1016/j.snb.2021.129585.
[40] Y. Sun, F. Zhang, L. Xu, Z. Yin, X. Song, Roughness-controlled copper nanowires and Cu nanowires–Ag heterostructures: synthesis and their enhanced catalysis, J. Mater. Chem. A 2 (2014) 18583–18592, https://doi.org/10.1039/c4ta03689a.
[41] P. Zhang, C. Shao, Z. Zhang, M. Zhang, J. Mu, Z. Guo, et al., In situ assembly of well-dispersed Ag nanoparticles (AgNPs) on electrospun carbon nanofibers (CNFs) for catalytic reduction of 4-nitrophenol, Nanoscale 3 (2011) 3357, https://doi.org/10.1039/c1nr10405e.
[42] G. Ma, X. Yan, Y. Li, L. Xiao, Z. Huang, Y. Lu, et al., Ordered nanoporous silica with periodic 30–60 nm pores as an effective support for gold nanoparticle catalysts with enhanced lifetime, J. Am. Chem. Soc. 132 (2010) 9596–9597, https://doi.org/10.1021/ja1027524.
[43] Y. Borodko, P. Ercius, V. Pushkarev, C. Thompson, G. Somorjai, From single Pt atoms to Pt nanocrystals: photoreduction of Pt^{2+} inside of a PAMAM dendrimer, J. Phys. Chem. Lett. 3 (2012) 236–241, https://doi.org/10.1021/jz201599u.
[44] C. Fang, J. Hu, X. Jiang, Z. Cui, X. Xu, T. Bi, Bifunctional PtCu electrocatalysts for the N_2 reduction reaction under ambient conditions and methanol oxidation, Inorg. Chem. Front. 7 (2020) 1411–1419, https://doi.org/10.1039/d0qi00035c.
[45] F.J. Perez-Alonso, D.N. McCarthy, A. Nierhoff, P. Hernandez-Fernandez, C. Strebel, I.E. Stephens, et al., The effect of size on the oxygen electroreduction activity of mass-selected platinum nanoparticles, Angew. Chem. Int. Ed. Engl. 51 (2012) 4641–4643, https://doi.org/10.1002/anie.201200586.
[46] V. Tripković, I. Cerri, T. Bligaard, J. Rossmeisl, The influence of particle shape and size on the activity of platinum nanoparticles for oxygen reduction reaction: a density functional theory study, Catal. Lett. 144 (2014) 380–388, https://doi.org/10.1007/s10562-013-1188-y.
[47] M. Abdinejad, S. Subramanian, M.K. Motlagh, M. Noroozifar, S. Duangdangchote, I. Neporozhnii, et al., Insertion of MXene-based materials into Cu–Pd 3D aerogels for electroreduction of CO_2 to formate, Adv. Energy Mater. 13 (2023) 2300402, https://doi.org/10.1002/aenm.202300402.
[48] B. Liu, B. Ran, C. Chen, L. Shi, J. Jin, Y. Zhu, High-throughput microfluidic production of bimetallic nanoparticles on MXene nanosheets and application in hydrogen peroxide detection, ACS Appl. Mater. Interfaces 14 (2022) 56298–56309, https://doi.org/10.1021/acsami.2c16316.
[49] D.C. Zhong, Y.N. Gong, C. Zhang, T.B. Lu, Dinuclear metal synergistic catalysis for energy conversion, Chem. Soc. Rev. 52 (2023) 3170–3214, https://doi.org/10.1039/d2cs00368f.
[50] S. Gu, S. Risse, Y. Lu, M. Ballauff, Mechanism of the oxidation of 3,3′,5,5′-tetramethylbenzidine catalyzed by peroxidase-like Pt nanoparticles immobilized in spherical polyelectrolyte brushes: a kinetic study, ChemPhysChem 21 (2020) 450–458, https://doi.org/10.1002/cphc.201901087.
[51] Y. Lei, X. He, Y. Zeng, X. Wang, L. Yang, X. Liu, et al., Pt-S bond stabilized DNAzyme nanosensor with thiol-resistance enabling high-fidelity biosensing, Talanta 276 (2024) 126187, https://doi.org/10.1016/j.talanta.2024.126187.

Jun Tan is currently a graduate student of Hainan Medical University. Her research interest is the development of biosensing strategy for clinical diagnosis of tropical diseases.

Nini Luo is currently a graduate student of Hainan Medical University. Her research interest is the development of biosensing strategy for clinical diagnosis of tropical diseases.

Ting Zhang is currently a professor of Hainan Medical University. Her main research interests is molecular mechanism of pathogen host interaction.

Juan Yao is currently a graduate student of Hainan Medical University. Her research interest is the development of biosensing strategy for clinical diagnosis of tropical diseases.

Xuemiao Li is currently a graduate student of Hainan Medical University, Studying on the therapeutic mechanism of tropical pathogens.

Yanshuang Wang is currently working in the Second Affiliated Hospital of Hainan Medical University. Her research interest is the development of biosensing strategy for clinical diagnosis of tropical diseases.

Guozhen Tian is currently working in Hainan Women and Children's Medical Center. His research interest is the development of biosensing strategy for clinical diagnosis of tropical diseases.

Hua Pei is currently working in the Second Affiliated Hospital of Hainan Medical University. His research interest is the development of biosensing strategy for clinical diagnosis.

Qizhi Diao is currently working in Hainan Branch of Shanghai Children's Medical Center. His research interest is the development of biosensing strategy for clinical diagnosis.

Huangxian Ju is a Changjiang Professor and the director of State Key Laboratory of Analytical Chemistry for Life Science in Nanjing University. His research interests focus on bioanalytical chemistry, nanobiosensing and molecular diagnostics. He has published 13 books and 918 papers in different journals with SCIE h-index of 106 (>44,300 citations) and Google Scholar h-index of 117 (> 53000 citations).

Qianfeng Xia is currently president of School of Tropical Medicine and Laboratory Medicine, Hainan Medical University. His research interests focus on the novel methods and key technologies for clinical molecular diagnostic testing, tropical disease prevention and control. He has published more than 50 papers as the first or corresponding author.